sensors

MDPI

Article

Compact Double-Layer FR4-Based Focusing Lens Using High-Efficiency Huygens' Metasurface Unit Cells

Kd M. Raziul Islam and Sangjo Choi *

Department of Electrical Engineering, University of Ulsan, Ulsan 44610, Korea; 20195153@mail.ulsan.ac.kr
* Correspondence: sangjoc@ulsan.ac.kr

Received: 29 July 2020; Accepted: 26 October 2020; Published: 28 October 2020

Abstract: High transmission efficiency metasurface unit cells have been designed based on surface electric and magnetic impedances derived from Huygens' principle. However, unit cells for low transmission loss (<1 dB) over a wide transmission phase range require at least three metallic layers, which complicates the unit cell design process. In this paper, we introduce high-efficiency Huygens' metasurface unit cell topologies in double-layer FR4 printed circuit board (PCB) by implementing surface electric and magnetic current using the top and bottom metallic patterns and via drills. Eleven unit cells were optimized for wide phase coverage (−150° to 150°) with a low average transmission loss of −0.82 dB at 10 GHz. To demonstrate the high-efficiency of the designed unit cells, we designed and fabricated two focusing lenses with dimensions of near 150 × 150 mm (5λ × 5λ) to focus a spherical beam radiated from short focal distances (f = 100 and 60 mm). The fabricated focusing lens showed 12.87 and 13.58 dB focusing gain for f = 100 and 60 mm at 10 GHz, respectively, with a 1 dB fractional gain bandwidth of near 10%. We expect that the proposed focusing lens based on high-efficiency double-layer metasurface unit cells can help realize compact and high-gain focusing lens-integrated antenna systems.

Keywords: metasurface; focusing lens; Huygens' principle; surface electric and magnetic currents

1. Introduction

Metasurface is a two-dimensional structure with subwavelength particles or unit cells for manipulating propagation direction [1–5], polarization [6–11], and orbital angular momentum (OAM) [12–15] of electromagnetic (EM) waves. The ground-breaking feature from the metasurface was introduced from extensive review papers [16–20], and metasurface-based lenses [21–23], antennas [24–27], and holographic imaging [28,29] have been actively studied. After the advent of a popular metasurface design using the generalized Snell's law [1], which deals with a phase gradient (scalar) on the surface, Huygens' principle was utilized to improve the efficiency of wave-refracting metasurfaces by introducing surface electric and magnetic currents (vector quantities) [2]. Using Huygens' principle, a metasurface was modeled as a two-dimensional boundary and the required electric and magnetic surface impedances to control the propagation direction of a transmitted wave were achieved [2]. Metasurface design based on Huygens' principle is theoretically sound; however, it is not straightforward to implement electric and magnetic surface impedances that cover a wide transmission phase range with high transmission efficiency in a planar 2D structure, e.g., printed circuit board (PCB). In [2], Pfeiffer et al. designed electric and magnetic dipoles in two-layer PCB strips, but had to stack the strips between air space to align the vector components of the incident electric and magnetic fields with the corresponding surface impedance vectors. More fabrication-friendly unit cells with the required surface impedances have been designed and laid out in two-layer PCBs, but the unit cells were not able to maintain

low transmission loss (<1 dB) for all the required surface impedances, especially high electric and magnetic resonance cases [30–37]. For better efficiency, a three-layer PCB capable of generating a loop current from the first and third layers using two vias was implemented [38–40]. Recently, in the same three-layer PCBs, symmetric and asymmetric unit cells with two magnetic dipoles (dogbone shape) on the top and bottom layer and an electric dipole (capacitor-loaded dipole) in the middle layer have been implemented [25,26,41,42]. Despite the higher transmission efficiency of these three-layer unit cells, the drawbacks can be increased geometrical parameters that need to be tuned and interference by waves propagating along the multiple layers, which require optimization.

In this paper, we introduce double-layer metasurface unit cells with high transmission efficiency and wide phase coverage at 10 GHz by constructing electric and magnetic dipole structures based on Huygens' principle. In the unit cells, electric and magnetic dipoles were implemented in 1.6 mm-thick (≈λ/18.8) double-layer FR4 PCB and via drills were used to form antisymmetric conducting loops for magnetic dipole resonance by connecting top and bottom metallic traces. Vias were also implemented in the electric dipole structure and the desired capacitance of the unit cell was achieved. Overall, we designed 11 unit cells to cover transmission phases from −150° to 150° and achieved a low average transmission loss of −0.82 dB at 10 GHz. To assess the practical performance of the unit cells, we designed two compact lenses with near 5λ × 5λ (152.1 × 156 mm) size to focus a spherical beam to specific focal points of 100 mm (f/D = 0.65) and 60 mm (f/D = 0.39). The lenses were designed for such low f/D values to be used for a compact and low profile transmitarray [43,44]. From the fabricated devices, radiated power from the half-wave dipole located at the focal distances was enhanced by 12.87 and 13.58 dB at 10 GHz for f/D = 0.65 and 0.39 cases, respectively, and a wide 1 dB gain bandwidth near 10% was demonstrated.

2. Huygens' Metasurface Unit Cell Design

2.1. Unit Cell Design Method

The generalized sheet transition condition (GSTC) models a metasurface as electric and magnetic polarizability densities (α_{ES} and α_{MS}) and relates those to the transmission coefficient (T) and reflection coefficients (R) of the metasurface [45]. Then, using Equations (1) and (2), α_{ES} and α_{MS} can be converted to the electric surface admittance (Y_{es}) and magnetic surface impedance (Z_{ms}), which are familiar concepts from Huygens' principle. Here, we assume isotropic surface electric admittance and magnetic impedance.

$$Y_{es} = j\omega\varepsilon\alpha_{ES} \tag{1}$$

$$Z_{es} = j\omega\mu\alpha_{MS} \tag{2}$$

By the simple conversion, the normalized values of $Y_{es}\eta_{00}$ and Z_{ms}/η_0 are given in terms of T and R in Equations (3) and (4). It is important to note that these simple equations can be derived when the propagation directions of the incident and transmitted waves are normal to the boundary [45]. More general equations with the arbitrary incident and transmitted angles were also derived in [46].

$$Y_{es}\eta_0 = 2\frac{1-T-R}{1+T+R} \tag{3}$$

$$Z_{ms}/\eta_0 = 2\frac{1-T+R}{1+T-R} \tag{4}$$

Here, η_0 is the intrinsic impedance of free space. Equations (3) and (4) indicate that a reflectionless (R = 0) metasurface requires the same values of $Y_{es}\eta_0$ and Z_{ms}/η_0. To maintain almost perfect transmission (T = 1) with wide transmission phase variation, only the imaginary part of Y_{es} and Z_{ms} should be utilized. Figure 1 shows that the simultaneous change of $\mathrm{Im}\{Y_{es}\eta_0\}$ and $\mathrm{Im}\{Z_{ms}/\eta_0\}$ from −15 to 15 covers transmission phases from −165° to 165°. Here, $Y_{es}\eta_0$ and Z_{ms}/η_0 are purely imaginary numbers.

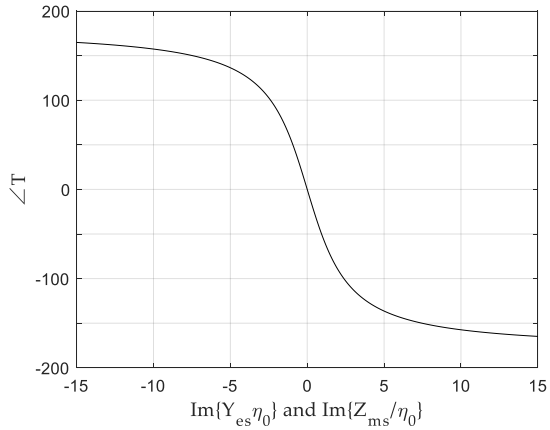

Figure 1. Transmission phases versus the imaginary part of the normalized surface electric admittance $I_m\{Y_{es}\eta_0\}$ and the normalized surface magnetic impedance $Im\{Z_{ms}/\eta_0\}$.

2.2. Unit Cell Topology Design and Analysis

We designed unit cells to provide desired normalized Y_{es} and Z_{ms} values to cover a wide range of transmission phases (−150° ~ 150°) with low transmission loss (<1 dB) at 10 GHz. Instead of using one topology for all the phases, we designed three optimum unit cell topologies for specific transmission phase ranges. First, we designed a unit cell with a high positive Y_{es} and Z_{ms} to realize the −150° transmission phase with low transmission loss. Generally, electric dipole resonance can be implemented easily with capacitor-like structures and is stronger than magnetic resonance. To increase magnetic resonance strength, which should match the electric resonance strength, we implemented two magnetic dipoles on the sides and one electric dipole at the center using vias, as shown in Figure 2.

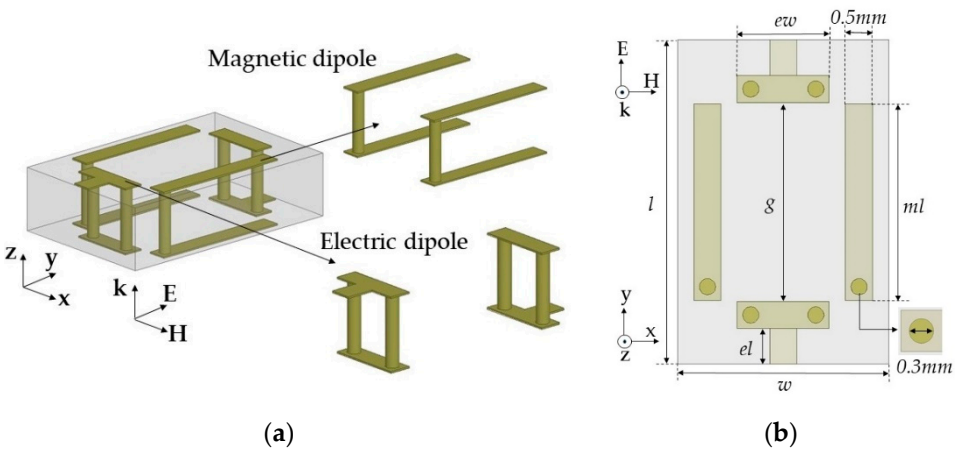

Figure 2. Electric and magnetic dipole in topology 1 from the (**a**) side–side view and (**b**) top view.

Here, the alignment of both dipoles was based on a y-polarized TEM wave propagating along the z-axis. The unit cells were simulated using Ansys high frequency structure simulator (HFSS) and the excitation and boundary conditions were used with wave ports and perfect electric conductor (PEC)/perfect magnetic conductor (PMC) boundaries, respectively. In the design, we used a 1.6 mm-thick double-layer FR4 substrate with a relative permittivity (ε_r) of 4.3 and loss tangent (tan δ) of 0.008. The unit cell area was fixed to a length (l) of 6 mm and width (w) of 3.9 mm. We used the rectangular-shaped unit cell to support long asymmetric current flow and a close space between the two magnetic dipoles to achieve a high Z_{ms} value and a low discretization error along the x-axis. Geometrical parameters of the unit cell included ml (the length for the magnetic dipole), g (the gap between the capacitively coupled electric dipoles), and ew (the width of the capacitor of the electric dipoles). Last, el indicates the electric dipole length, which is dependent on g. Therefore, we varied ml

for the desired Y_{es} values and g and ew for the Y_{es} tuning. One benefit of this unit cell topology is that electric and magnetic resonance can be controlled independently because both electric and magnetic structures are implemented perpendicularly by the intuition of Huygens' surface electric and magnetic currents. Finally, a unit cell with ml = 3.64 mm, g = 3.68 mm, and ew = 1.7 mm achieved high Y_{es} and Z_{ms} values of 7.55 and 5.87, respectively, with an S_{21} of −0.96 dB and −150° transmission phase. To balance Y_{es} and Z_{ms}, Y_{es} resonance where the peak of Y_{es} occurs has to be located near 12.4 GHz, which was implemented with lower capacitance by using a wide gap distance (g = 3.68 mm) between the two electric dipoles, as shown in Figure 3b. However, the Z_{ms} resonance should be near 10 GHz to achieve a sufficiently high Z_{ms} value to match the Y_{es} value at 10 GHz. Figure 3c shows a high magnetic field excited along the x-axis due to current flows on the magnetic dipoles.

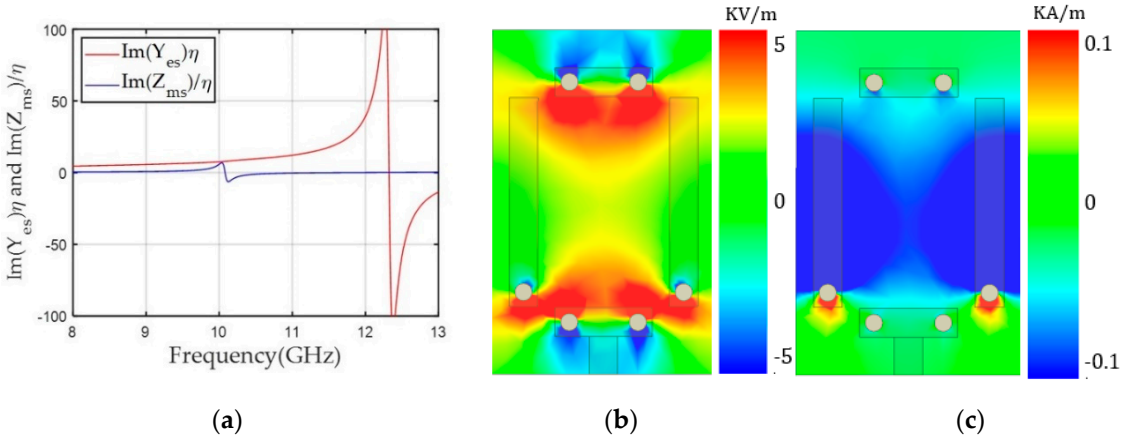

Figure 3. (**a**) Y_{es} and Z_{ms} values of the unit cell according to frequency for a transmission phase of −150°. (**b**) The y component of the electric field (E_y). (**c**) The x component of the magnetic field (H_x) along the x-y plane in the middle of the unit cell at 10 GHz.

Next, we reduced the Y_{es} and Z_{ms} resonance frequencies to achieve balanced negative values for both Y_{es} and Z_{ms} at 10 GHz for the +150° transmission phase, as shown in Figure 4a. Based on the unit cell with a transmission phase of –150°, the gap (g) of the electric dipole was lowered up to 1.30 mm and the magnetic dipole length (ml) was decreased to 3.61 mm. This structure moved the Y_{es} and Z_{ms} resonance frequencies to 8.2 and 9.8 GHz, respectively, and achieved balanced Y_{es} (−7.19) and Z_{ms} (−7.15) at 10 GHz, providing −1.1 dB S_{21} with +150° phase. Figure 4b,c shows the unit cell structure for the +150° phase and E_y and H_x on the x–y plane in the middle of the structure. E_y was confined near the gap of the electric dipole's capacitor structure, which was responsible for the lower resonance frequency of Y_{es} compared to the unit cell for the −150° phase. Figure 4c shows that the strong x components of the magnetic field were distributed in the middle of the magnetic dipoles, lowering the resonance frequency of Z_{ms} and yielding a negative Z_{ms} value at 10 GHz.

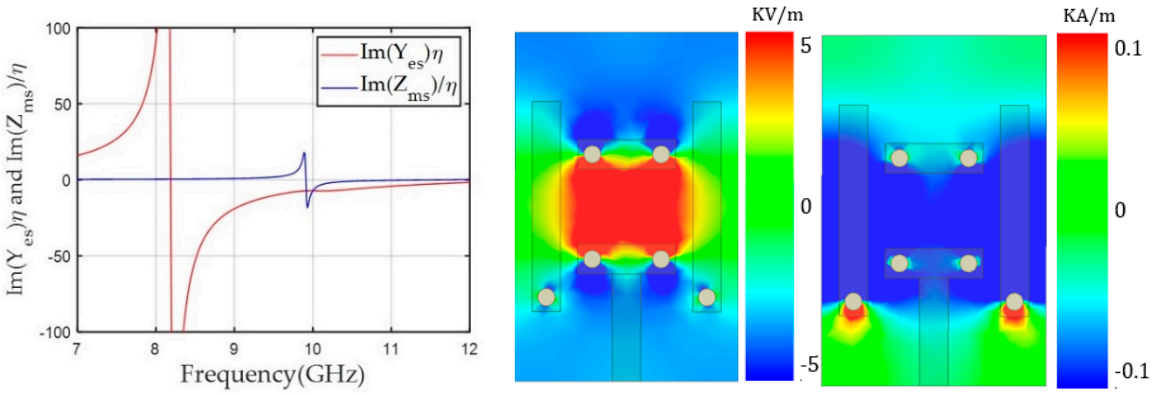

(**a**) (**b**) (**c**)

Figure 4. (**a**) Y_{es} and Z_{ms} values of the unit cell along frequency for a transmission phase of +150°. (**b**) The y component of the electric field (E_y). (**c**) The x component of the magnetic field (H_x) along the x-y plane in the middle of the unit cell at 10 GHz.

We realized the unit cells for the other positive phases from +120° to 0° by lowering negative Y_{es} and Z_{ms} values at 10 GHz. To do that, we lowered the resonance frequency of Y_{es} and Z_{ms} by reducing the gap of the electric dipole (g) and tuning the electric dipole width (ew), and increasing the length of the magnetic dipole (ml), respectively. Figure 5a shows the normalized Y_{es} and Z_{ms} values from the unit cell for +120° with g = 0.37 mm, ew = 1.0 mm, and ml = 3.70 mm. The balanced Y_{es} and Z_{ms} values of −3.5 and −3.3 at 10 GHz are shown; this condition provided a low S_{21} of −1.1 dB. As shown in Figure 5b,c, E_y and H_x from the unit cell with +120° had a similar confined E_y field near a smaller gap of the electric dipole and stronger magnetic field due to a longer ml compared to the unit cell for the +150° phase. This phenomenon corresponded to lower Y_{es} and Z_{ms} resonance frequencies in the +120° phase structure. We decreased the Y_{es} and Z_{ms} resonance frequencies by using a more confined E_y and higher H_x, and finally covered phases from +90° to 0°. Detailed geometries and Y_{es} and Z_{ms} values are shown in Table 1.

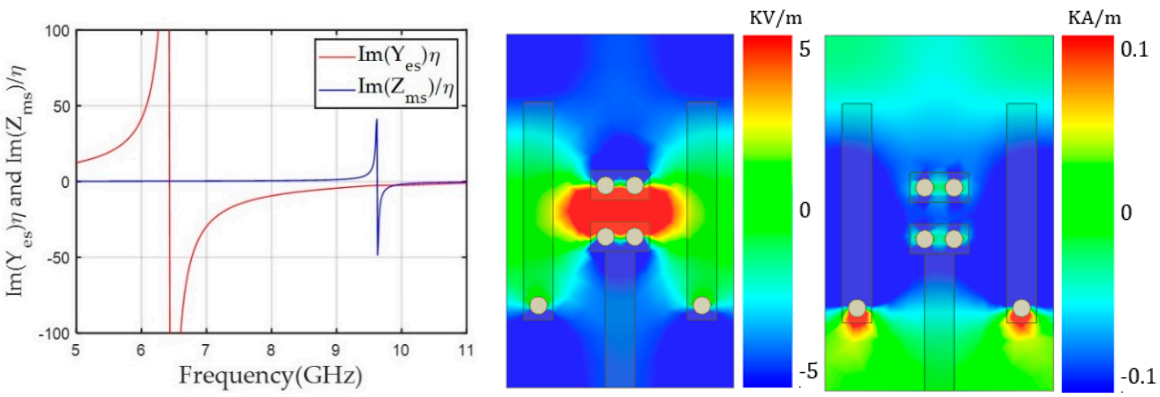

(**a**) (**b**) (**c**)

Figure 5. (**a**) Y_{es} and Z_{ms} values of the unit cell according to frequency for a transmission phase of +120°. (**b**) The y component of the electric field (E_y). (**c**) The x component of the magnetic field (H_x) along the x-y plane in the middle of the unit cell at 10 GHz.

Table 1. Geometric parameters, simulated electric surface admittance (Y_{es}), magnetic surface impedance (Z_{ms}), transmission phases, and transmission loss of the 11 metasurface unit cells with topologies 1, 2, or 3.

Cell	Topology	g (mm)	g1 (mm)	g2 (mm)	ml (mm)	ew (mm)	Im (Y_{es})	Im (Z_{ms})	Trans. Phase (°)	Trans. Loss (dB)
1	1	0.20			4.60	1.7	0	0	0	−0.4
2	1	0.20			4.15	1.7	−1.1	−0.2	30	−1.1
3	1	0.20			3.72	2.1	−1.5	−0.9	60	−1.0
4	1	0.20			3.76	1.0	−2.4	−1.7	90	−1.0
5	1	0.37			3.70	1.0	−3.5	−3.3	120	−1.1
6	1	1.30			3.61	1.7	−7.19	−7.15	150	−1.1
7	1	3.68			3.64	1.7	7.55	5.87	−150	−0.96
8	1	4.60			3.61	1.7	3.9	2.8	−120	−0.72
9	2				3.47	2.0	2.8	1.4	−90	−0.72
10	3		0.5	0.8	3.6		1.4	0.88	−60	−0.59
11	3		1	0.6	2.8		0.7	0.4	−30	−0.34

For negative transmission phases, we used the unit cell for −150° and achieved −120° by increasing the Y_{es} and Z_{ms} resonance frequencies. For lower effective capacitance and inductance of the unit cell, the gap (g) between the electric dipole was increased from 3.68 to 4.60 mm and the magnetic dipole length (ml) was shortened from 3.64 to 3.61 mm. Finally, lower positive Y_{es} (3.9) and Z_{ms} (2.8) values at 10 GHz were achieved with a low S_{21} of −0.72 dB. Figure 6a shows the Y_{es} and Z_{ms} values according to frequency for the unit cells for the −150° and −120° phases. Lower Y_{es} and Z_{ms} values were observed for the −120° case at 10 GHz due to the higher Y_{es} resonance frequency near 14.8 GHz. The lower Z_{ms} value in the −120° case was due to a resonance frequency shift to a higher frequency near 10.2 GHz. Figure 6b shows that E_y for the unit cell with the −120° phase was distributed over a larger area than observed for the −150° case (Figure 3a). Figure 6c for H_x also shows lower magnetic fields between two magnetic dipoles. Both trends correspond to higher resonance frequencies for both Y_{es} and Z_{ms} and lower values at 10 GHz for the −120° case.

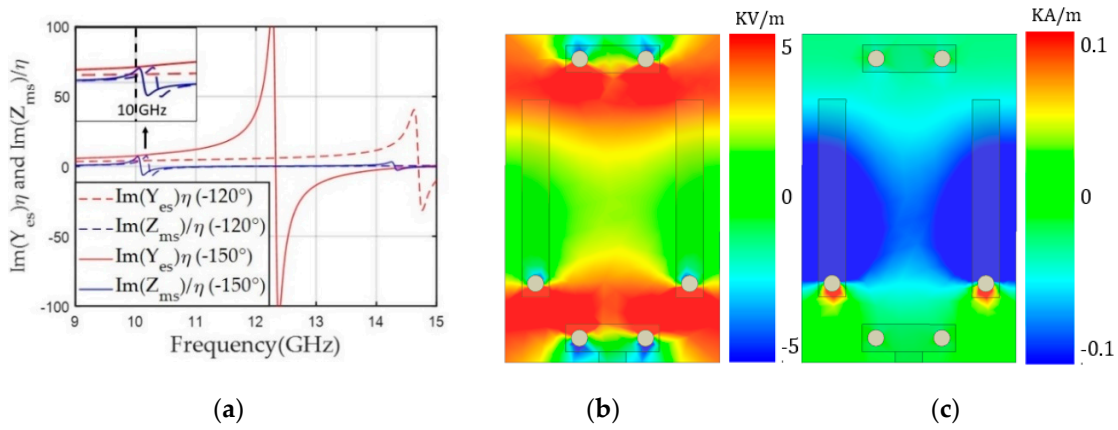

Figure 6. (**a**) Y_{es} and Z_{ms} values of the unit cell according to frequency for transmission phases of −150° and −120°. (**b**) The y component of the electric field (E_y) for the transmission phase of −120°. (**c**) The x component of the magnetic field (H_x) for −120° along the x-y plane in the middle of the unit cell at 10 GHz.

For the −90° transmission phase, lower positive Y_{es} and Z_{ms} are needed; however, the gap of the electric dipole (g) cannot be further increased due to fabrication limits. Therefore, we used one electric dipole structure to provide a lower Y_{es} at 10 GHz and two magnetic dipoles were maintained, as shown in Figure 7a. The geometrical parameters are shown in Figure 7b; an ew of 2 mm and ml of 3.47 mm provided a normalized Y_{es} of 2.8 and Z_{ms} of 1.4, resulting in the achievement of a −90° phase

with a low S_{21} of −0.72 dB. Figure 7c shows that Y_{es} and Z_{ms} values became lower at 10 GHz due to Z_{ms} and Y_{es} resonance frequencies higher than 10 GHz. Figure 7d,e shows that E_y was distributed over a larger area and H_x was weaker in the −90° case than the −120° case.

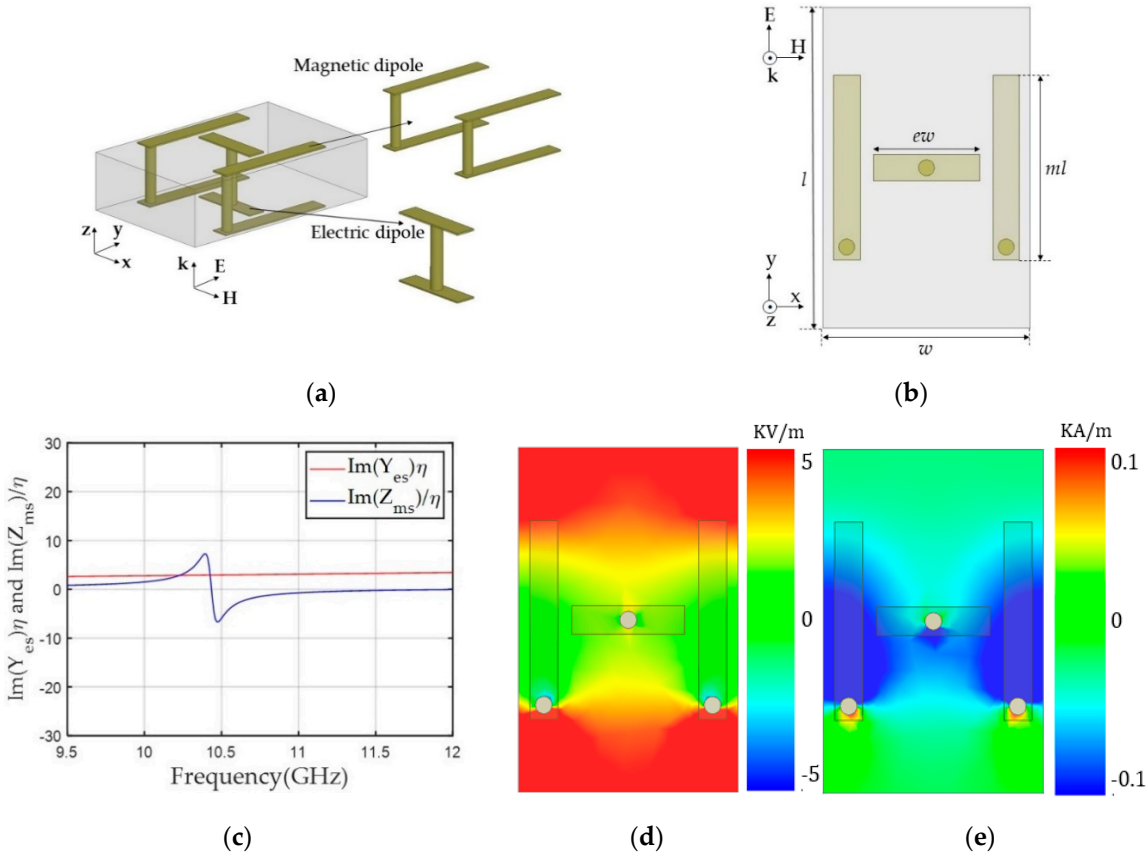

Figure 7. Electric and magnetic dipoles in the topology 2 structure from the (**a**) side-side view and (**b**) top view. (**c**) Y_{es} and Z_{ms} values of the unit cell according to frequency for a transmission phase of −90°. (**d**) The y component of the electric field (E_y). (**e**) The x component of the magnetic field (H_x) along the x-y plane in the middle of the unit cell at 10 GHz.

To further reduce Y_{es} and Z_{ms} to cover the −60° and −30° transmission phases, we used one magnetic dipole in the center of the unit cell and located the electric dipoles around the boundary of the unit cell on the top and bottom layers, as shown in Figure 8a. Figure 8b shows the geometrical parameters of topology 3. The length of g3 was fixed at 0.5 mm and horizontal gaps (g1 and g2) between the magnetic and the electric dipole structures, and magnetic dipole length (ml) were mainly tuned to control the near-zero Y_{es} and Z_{ms} accurately such that Y_{es} and Z_{ms} became 0.7 and 0.4 for the −30° case. Here, ml and g2 determine the vertical length of the electric dipole. Finally, we achieved almost zero transmission loss for the −30° and −60° cases (−0.34 and −0.59 dB, respectively). This topology achieved near-zero Y_{es} values at 10 GHz because maximum Y_{es} resonance frequencies were located under 8 GHz and the zero-crossing Y_{es} frequency was near 10 GHz, as shown in Figure 9a,b. Similar to the other negative phase cases, Z_{ms} resonance frequencies were higher than 10 GHz, resulting in near-zero Z_{ms} values at 10 GHz. Figure 9c,d shows that E_y was distributed along the entire area of the unit cells for transmission phases of −60° and −30°, in contrast to the other negative phase cases. We attributed the wide distribution of E_y to the near-zero Y_{es} at 10 GHz for both cases. Compared to the −60° case, the −30° case showed a more distributed E_y; therefore a slightly higher Y_{es} value was achieved in the −60° case. Figure 9e,f shows that the −60° case had higher magnetic fields along the x-axis, resulting in a higher Z_{ms} value at 10 GHz.

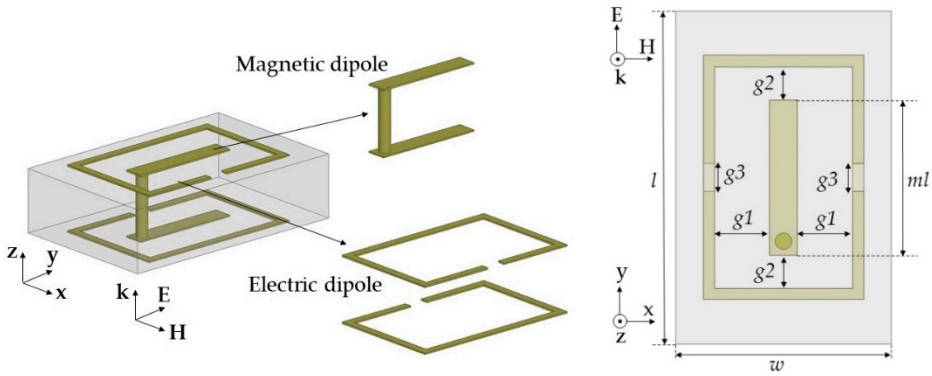

(**a**) (**b**)

Figure 8. Electric and magnetic dipoles in the topology 3 structure from the (**a**) side–side view and (**b**) top view.

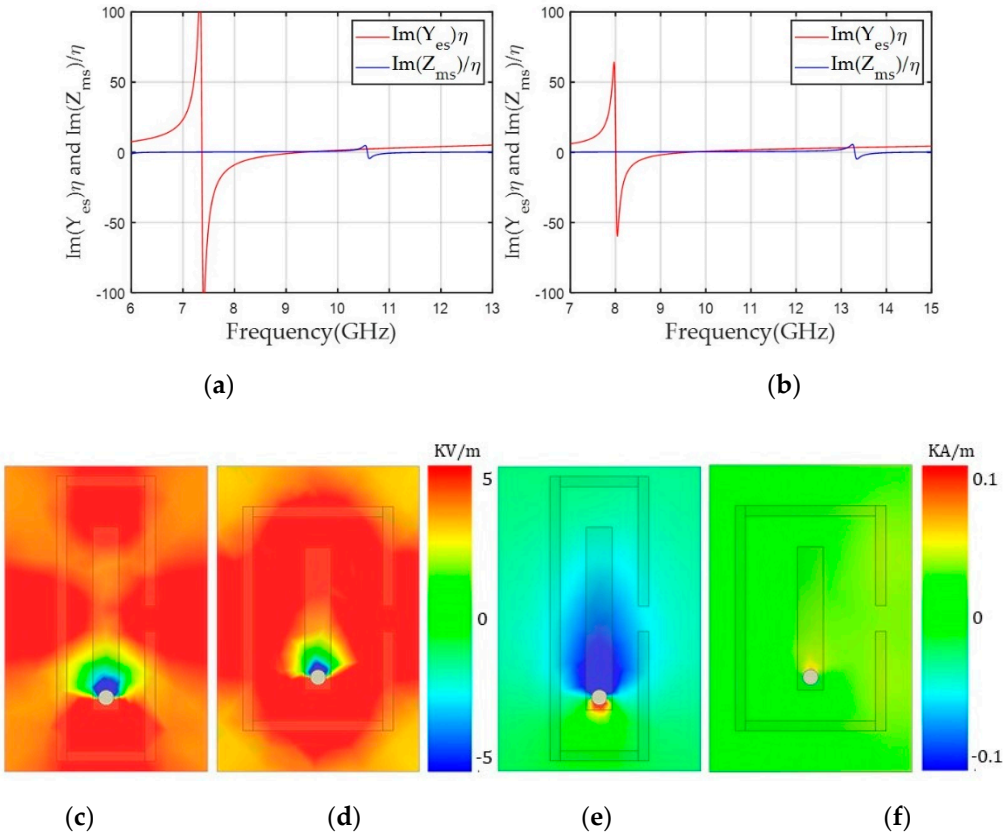

(**a**) (**b**)

(**c**) (**d**) (**e**) (**f**)

Figure 9. Y_{es} and Z_{ms} values of the unit cell according to frequency for transmission phases of (**a**) −60° and (**b**) −30°. The y component of the electric field (E_y) for transmission phases of (**c**) −60° and (**d**) −30°. The x component of the magnetic field (H_x) for transmission phases of (**e**) −60° and (**f**) −30° along the x-y plane in the middle of the unit cell at 10 GHz.

Figure 10 provides a top view of all the unit cells with topologies 1, 2, or 3. Y_{es} and Z_{ms} values of the corresponding unit cells and their transmission parameters are presented in Table 1. The highest and lowest transmission loss levels were −1.1 and −0.34 dB, respectively, and the average loss was −0.82 dB, which was lower than the average S_{21} of −1.04 dB reported for a similar double-layer PCB-based unit cell operating at 10 GHz [32]. Moreover, previously reported structures had a maximum transmission loss of −2.5 dB, while that of the proposed unit cells was −1.1 dB. These findings demonstrate that unit cell topologies optimized for specific transmission phases significantly reduce transmission loss of the overall unit cells.

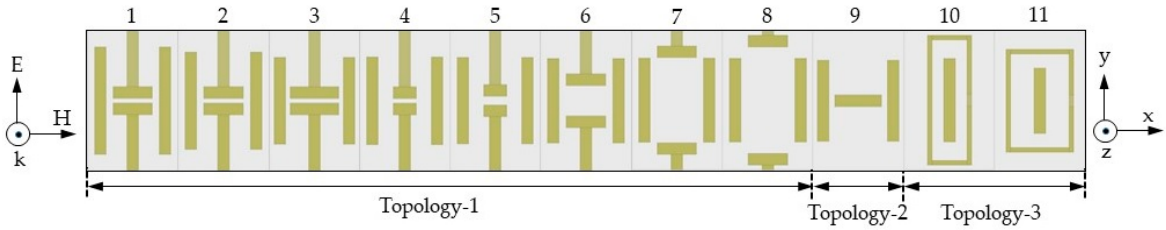

Figure 10. Top view of 11 unit cells with topologies 1, 2, or 3.

2.3. Focusing Lens Design

Based on the high transmission efficiency of the 11 unit cells covering the −150° to 150° phases, we designed two focusing lens structures to collimate incident spherical waves radiated from short distances. Because the designed unit cells had subwavelength dimensions of w = 3.9 mm (λ/7.7) and l = 6 mm (λ/5), we were able to design a compact-sized (5λ × 5λ) array with short focal points (f) of 100 and 60 mm. Both 100 and 60 mm focal points means low f/D numbers of 0.65 and 0.39, respectively, that would be needed for a compact focusing lens-integrated system. The required transmission phases (ϕ_i) to collimate the spherical waves from both focal points were determined from Equation (5), as shown in Figure 11a,b, and the corresponding unit cells were arranged accordingly. The target phases, drawn in Figure 11a,b, were discretized using 30° steps.

$$\phi_i = k_0(R_i - f) + \phi_0 \tag{5}$$

In Equation (5), R_i is the distance between the center of the unit cell element and the focal point and f is the focal distance. We used the wavenumber (k_0) from the 10 GHz frequency and set ϕ_0 to −150° as the default phase at the center of the array where R_i and f are equal. One thing to note is that due to the unit cells' compact size, steeper phase changes required for short focal distances could be realized with a low discretization error. Finally, we arranged different numbers of rectangular-shaped (3.9 × 6 mm) unit cells along the x-axis (39 cells) and y-axis (26 cells) to realize a near 5λ × 5λ-sized (152.1 × 156 mm) focusing lens. Figure 11c,d shows the implemented phase distribution of both focusing lenses. Because the calculated phases near the center of the focusing lenses were located in the middle of the 30° phase gap of the unit cells, a slight phase difference between Figure 11a,b and Figure 11c,d near the center area was allowed in the design process.

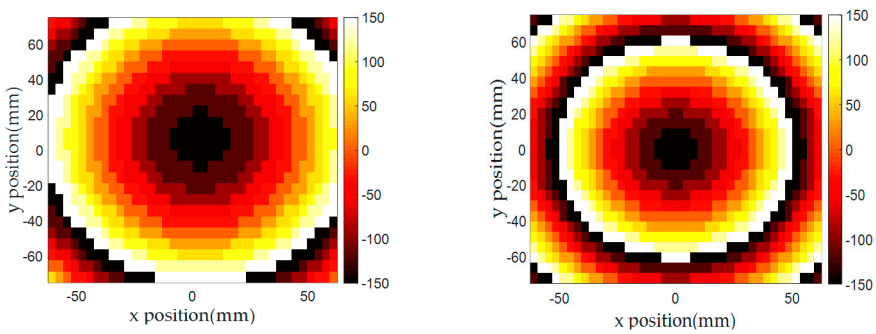

(**a**) (**b**)

Figure 11. *Cont.*

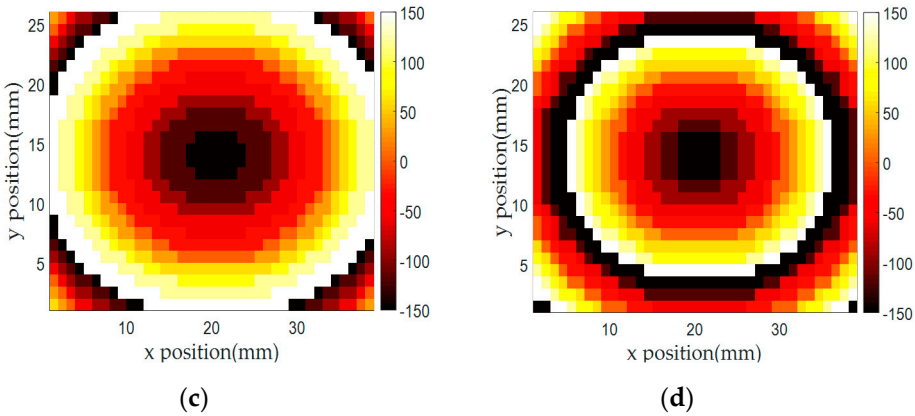

Figure 11. Required phase distributions calculated from Equation (5) of the focusing lens with (**a**) 100 mm and (**b**) 60 mm focal distances. Implemented phase distributions of the focusing lens with (**c**) 100 mm and (**d**) 60 mm focal distances.

In simulations, both focusing lenses with 3D unit cell structures were implemented in HFSS and the focusing gain was calculated. For the simulation load reduction, a quarter of the focusing lens in the first quadrant was used with symmetric boundaries in the simulation tool (see Figure 12). A spherical wave as the incident wave was implemented by a half-wave dipole antenna operating at 10 GHz at a focal distance from the focusing lens. The focusing gain, defined as the gain from the focusing lens–combined dipole antenna minus the gain of the dipole antenna at the boresight [47–49] was calculated as 13.47 and 14.09 dB at 10 GHz for f = 100 and 60 mm, respectively. Gain patterns from the simulations were compared with those obtained experimentally (see below).

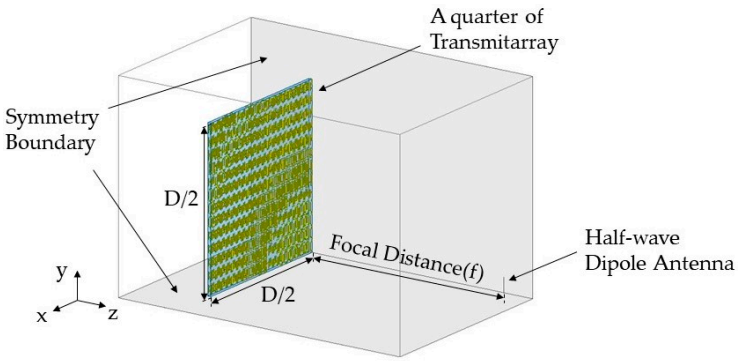

Figure 12. Simulation setup for the focusing lens with a half-wave dipole antenna as a feeding source in symmetry boundaries.

3. Fabrication and Measurement

For experimental verification, both focusing lenses with the same PCB size (156 × 160 mm) for f = 100 and 60 mm were fabricated, as shown in Figure 13a,b. Extra spaces on the boundary were added for stable patterns and via fabrication based on the designed size of 152.1 × 156 mm. Figure 13c shows the measurement setup; a focusing lens was fed by a half-wave dipole operating at 10 GHz at a specified focal distance and the focused beam from the array was captured by a standard horn antenna. The transmission coefficient (S_{21}) between the two antennas was measured using a vector network analyzer (Anritsu MS46122B, Anritsu Company, Morgan Hill, USA), and S_{21} values with and without the focusing lens were used to assess the focusing gain of the lens. For gain pattern measurements, the dipole antenna and the focusing lens were rotated horizontally in the same platform with a 1° step size and the measured pattern was compared with the simulation result. Distances between the dipole antenna and the focusing lens were maintained at the designed focal distances (100 and 60 mm).

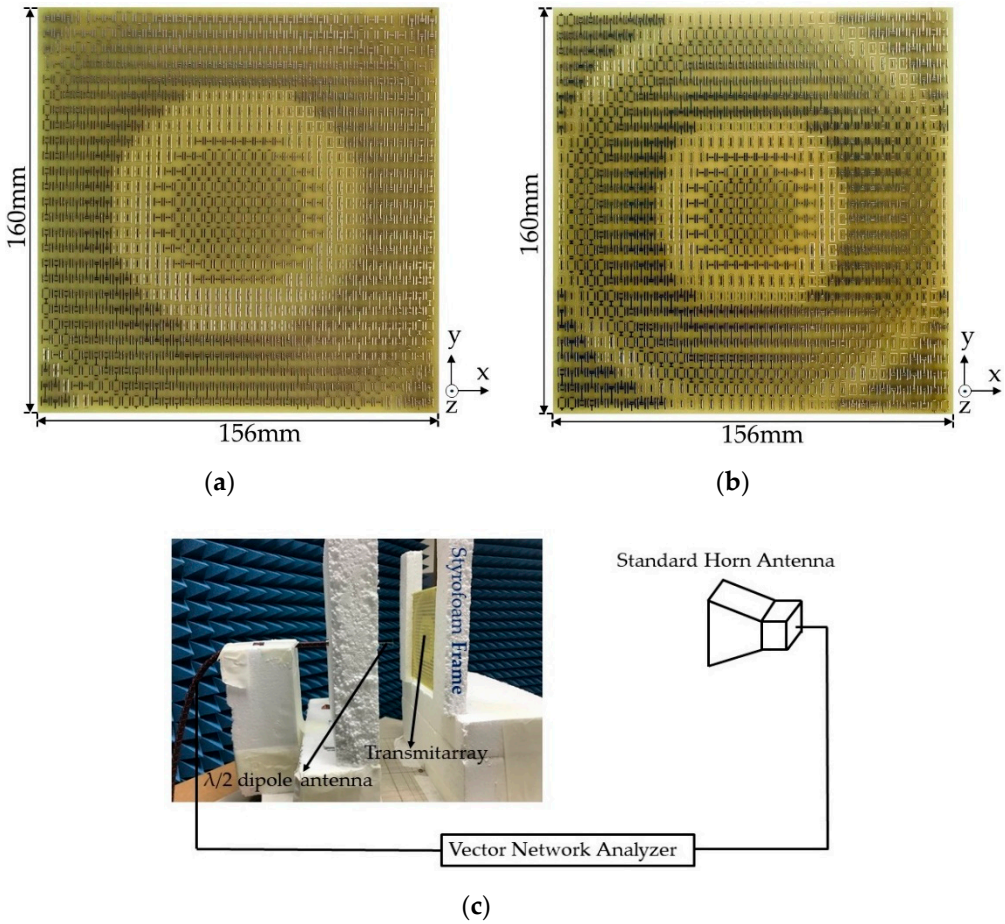

Figure 13. Top view of the fabricated focusing lenses with (**a**) 100 mm focal distance and (**b**) 60 mm focal distance. (**c**) Setup for measuring the focusing gain of the focusing lens using a half-wave dipole antenna as the feeding source and a standard horn antenna. Both antennas were connected to a vector network analyzer.

Figure 14a,b demonstrates that the measured focusing gain at the boresight and sidelobe levels of both focusing lens correlated well with the simulation results at 10 GHz. The main beams at the boresight provided a focusing gain of 12.87 dB for f = 100 mm and 13.58 dB for f = 60 mm, which are approximately 0.5 ~ 0.7 dB lower than the simulated results of 13.47 and 14.09 dB, respectively. We attributed this difference to fabrication uncertainty, e.g., substrate property deviation in the focusing lens and the nonideal spherical wave radiation from the half-wave dipole antenna. However, a near 13 dB focusing gain level from a lossy FR4-based compact focusing lens (5.1λ × 5.2λ) with a low f/D value of 0.39 is noteworthy. In Figure 14a, the discrepancy between both data in terms of the dip of the main lobe is noticeable and the reason should be slightly perturbed current distributions on the fabricated lens due to the aforementioned manufacture-related factors. Focusing gain at the boresight according to frequency was also measured and compared with the simulation results, as shown in Figure 14c,d. The measured data showed a slightly broader bandwidth compared to the simulated one with a wide 1-dB gain fractional bandwidth of near 10%.

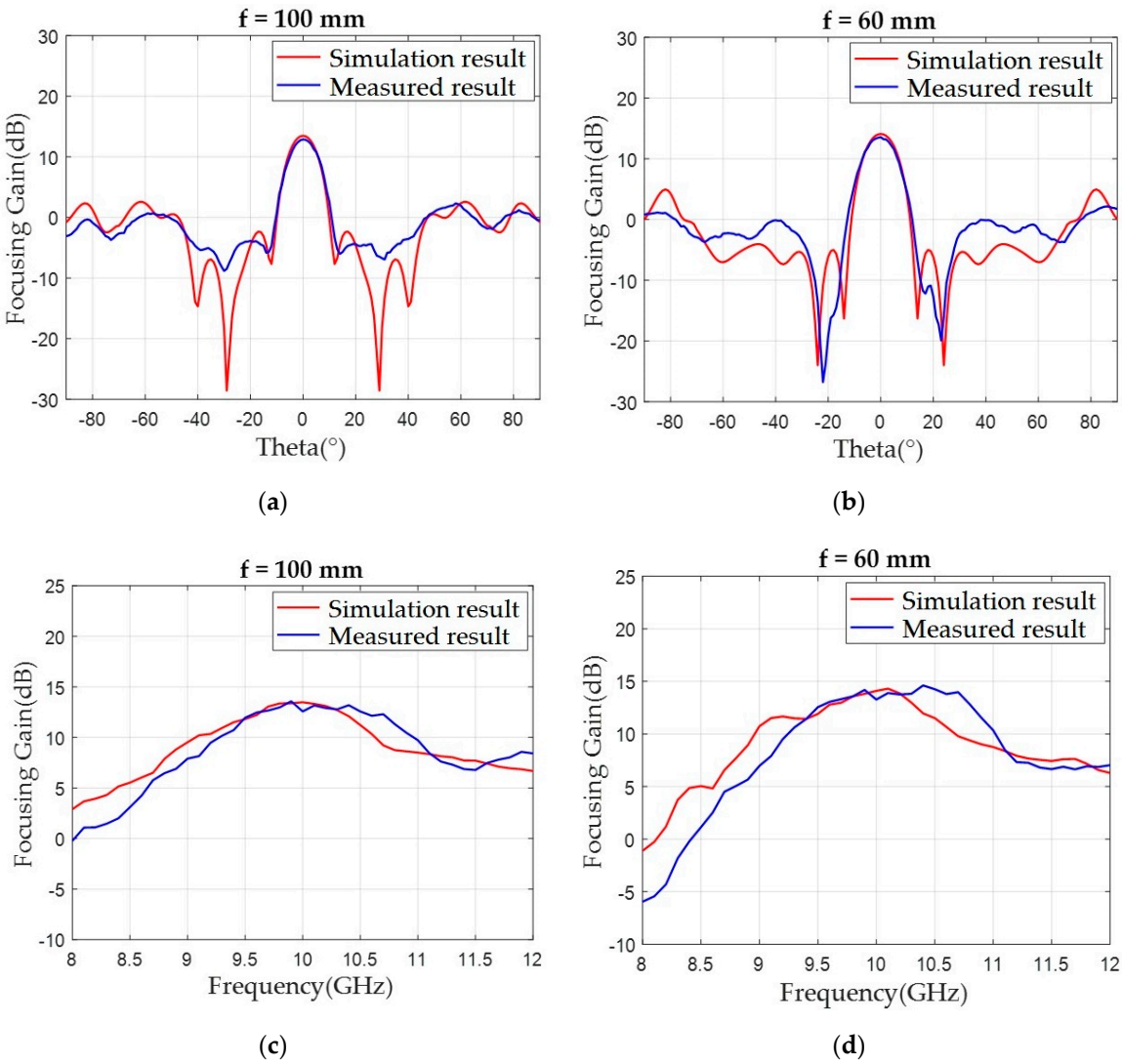

Figure 14. Simulated and measured and focusing gain patterns on the x-z plane with a function of theta at 10 GHz from the focusing lenses (**a**) with f = 100 mm and (**b**) with f = 60 mm. Simulated and measured focusing gain according to frequency from (**c**) f = 100 mm and (**d**) f = 60 mm.

4. Discussion and Conclusions

We designed high transmission efficiency metasurface unit cells operating at 10 GHz in a double-layer FR4 with a thickness of 1.6 mm (λ/18.8) for wide transmission phase coverage. The unit cells' physical structures were devised to implement perpendicularly directed surface electric and magnetic currents using the top and bottom metallic patterns and via drills. The proposed unit cells had three different topologies to control surface electric admittance (Y_{es}) and surface magnetic impedance (Z_{ms}) independently, providing compact (3.9 × 6.0 mm) 11 unit cells with an averaged −0.82 dB transmission loss and −150° ~ 150° transmission phases. Performance comparison with the referenced designs is shown in Table 2 and it is important to note that the designed unit cells achieved the lowest transmission loss even in a lossy FR4 (tan δ = 0.008) substrate compared to the recently reported double-layer unit cells from Table 2.

Table 2. Performance comparison of the proposed focusing lenses with the referenced designs.

Ref.	Layer #	Freq. (GHz)	Loss Tangent	Max. Loss of Unit Cell (dB)	Lens Size (mm × mm)	Thickness (mm)	Bandwidth (3 dB/1 dB)	f/D	Focusing Gain (dB)
[35]	2	20	0.0014	−1.75	338 × 338 (22.5λ × 22.5λ)	1.575 (λ/9.5)	-/5.9	1.24	14.9 [1]
[37]	2	28	0.0027	−1.63	165 × 165 (15.4λ × 15.4λ)	1.524 (λ/7.0)	13.3/-	0.95	16.4
[33]	2	26.2	0.001	−1.56	171.6 × 171.6 (15λ × 15λ)	1.5 (λ/7.6)	15.7/-	0.99	15.7 [1]
[32]	2	13	0.0037	−2.5	328 × 328 (14.2λ × 14.2λ)	0.762 (λ/30)	3/-	0.8	11.5
[34]	2	10	0.005	−3	360 × 500 (12λ × 16.6λ)	2 (λ/15)	6/-	0.3	7.65
[50]	3	10.2	0.004	−2.75	376.5 × 376.5 (12.8λ × 12.8λ)	1.1 (λ/26.7)	9.8/-	0.8	14.4
[36]	2	6	-	−1.4	210 × 210 (4.2λ × 4.2λ)	2 (λ/25)	15/-	0.8	9
[31]	2	10	0.001	−1.4	104 × 104 (3.46λ × 3.46λ)	3 (λ/10)	-/-	0.29	8.2
This Work	2	10	0.008	−1.1	156 × 160 (5.1λ × 5.2λ)	1.6 (λ/18.8)	20/10	0.65/ 0.39	12.87/ 13.58

[1] Focusing gain was calculated using the simulated gain from the feeding antenna.

To assess the efficiency of the proposed unit cells experimentally, we designed two focusing lenses with a size of 156 × 160 mm (5.1λ × 5.2λ) to focus a radiated spherical beam in short focal distances (f = 100 and 60 mm). We expected the compact unit cell to maintain a low discretization error with low f/D numbers (f/D = 0.65 and 0.39), which required steep phase variation in the focusing lens design. The fabricated focusing lenses boosted the half-wave dipole's gain more than 13 dB despite the short focal distances and achieved a wide 1-dB gain bandwidth of near 10%. Moreover, the focusing gain was increased by 0.7 dB with a focal distance change from 100 to 60 mm, demonstrating the low discretization error of the designed unit cells. From Table 2, the focusing gain levels of this work were lower within 3 dB compared to at least four times larger lenses in terms of center wavelength (λ), proving the higher focusing efficiency. Two slightly smaller lenses also showed 4 ~ 5 dB lower focusing gain values, and specifically, in [31], a compact (3.5λ × 3.5λ) and double-layer focusing lens with a low f/D of 0.29 showed focusing gain of 8.2 dB at 10 GHz. For a fair comparison, the aperture efficiencies using the measured focusing gain were calculated and a higher value of 6.88% from this work compared to 4.37% from [31] was shown. The higher efficiency from the designed lenses corresponds to the lower transmission loss from the proposed unit cells and manifests that higher spillover loss due to the broad radiation from the dipole antenna compared to the high gain patch antenna from [31] was also recovered. Moreover, the lens from [31] utilized narrow lateral dimensions for the phase coverage; it is thus subject to the narrow bandwidth (it was not reported). Finally, we expect that the high gain focusing lens with a low f/D based on the FR4-based high-efficiency double-layer unit cells can be utilized for low-profile beam-forming antenna systems in 5G and millimeter-wave communications.

Author Contributions: K.M.R.I. conducted the numerical simulations and designed the structures. S.C. conceived and supervised the research. All authors have read and agreed to the published version of the manuscript.

Funding: This work was supported by a National Research Foundation of Korea (NRF) grant funded by the Korea government (MSIT) (No. 2020R1C1C101209911).

Conflicts of Interest: The authors have no conflict of interest to declare.

References

1. Yu, N.; Genevet, P.; Kats, M.A.; Aieta, F.; Tetienne, J.-P.; Capasso, F.; Gaburro, Z. Light Propagation with Phase Discontinuities: Generalized Laws of Reflection and Refraction. *Science* **2011**, *334*, 333–337. [CrossRef]
2. Pfeiffer, C.; Grbic, A. Metamaterial Huygens' surfaces: Tailoring wave fronts with reflectionless sheets. *Phys. Rev. Lett.* **2013**, *110*, 197401. [CrossRef] [PubMed]
3. Yu, N.; Genevet, P.; Aieta, F.; Kats, M.A.; Blanchard, R.; Aoust, G.; Tetienne, J.-P.; Gaburro, Z.; Capasso, F. Flat Optics: Controlling Wavefronts with Optical Antenna Metasurfaces. *IEEE J. Sel. Top. Quantum Electron.* **2013**, *19*, 4700423. [CrossRef]
4. Liu, S.; Cheng, Q.; Xu, Q.; Wang, T.Q.; Du, L.L.; Luan, K.; Xu, Y.H.; Bao, D.; Fu, X.J.; Han, J.G.; et al. Free-Standing Metasurfaces for High-Efficiency Transmitarrays for Controlling Terahertz Waves. *Adv. Opt. Mater.* **2016**, *4*, 384–390. [CrossRef]
5. Pfeiffer, C.; Emani, N.K.; Shaltout, A.M.; Boltasseva, A.; Shalaev, V.M.; Grbic, A. Efficient Light Bending with Isotropic Metamaterial Huygens' Surfaces. *Nano Lett.* **2014**, *14*, 2491–2497. [CrossRef] [PubMed]
6. Pfeiffer, C.; Grbic, A. Bianisotropic Metasurfaces for Optimal Polarization Control: Analysis and Synthesis. *Phys. Rev. Appl.* **2014**, *2*, 044011. [CrossRef]
7. Pfeiffer, C.; Grbic, A. Cascaded metasurfaces for complete phase and polarization control. *Appl. Phys. Lett.* **2013**, *102*, 231116. [CrossRef]
8. Pfeiffer, C.; Zhang, C.; Ray, V.; Guo, L.J.; Grbic, A. High Performance Bianisotropic Metasurfaces: Asymmetric Transmission of Light. *Phys. Rev. Lett.* **2014**, *113*, 023902. [CrossRef] [PubMed]
9. Jia, S.L.; Wan, X.; Bao, D.; Zhao, Y.J.; Cui, T.J. Independent controls of orthogonally polarized transmitted waves using a Huygens metasurface. *Laser Photonics Rev.* **2015**, *9*, 545–553. [CrossRef]
10. Pfeiffer, C.; Grbic, A. Controlling Vector Bessel Beams with Metasurfaces. *Phys. Rev. Appl.* **2014**, *2*, 044012. [CrossRef]
11. Pfeiffer, C.; Zhang, C.; Ray, V.; Guo, L.J.; Grbic, A. Polarization rotation with ultra-thin bianisotropic metasurfaces. *Optica* **2016**, *3*, 427. [CrossRef]
12. Qin, F.; Wan, L.; Li, L.; Zhang, H.; Wei, G.; Gao, S. A Transmission Metasurface for Generating OAM Beams. *IEEE Antennas Wirel. Propag. Lett.* **2018**, *17*, 1793–1796. [CrossRef]
13. Jiang, S.; Chen, C.; Zhang, H.; Chen, W. Achromatic electromagnetic metasurface for generating a vortex wave with orbital angular momentum (OAM). *Opt. Express* **2018**, *26*, 6466. [CrossRef]
14. Chen, M.L.N.; Jiang, L.J.; Sha, W.E.I. Ultrathin Complementary Metasurface for Orbital Angular Momentum Generation at Microwave Frequencies. *IEEE Trans. Antennas Propag.* **2017**, *65*, 396–400. [CrossRef]
15. Zhang, K.; Wang, Y.; Yuan, Y.; Burokur, S.N. A Review of Orbital Angular Momentum Vortex Beams Generation: From Traditional Methods to Metasurfaces. *Appl. Sci.* **2020**, *10*, 1015. [CrossRef]
16. Holloway, C.L.; Kuester, E.F.; Gordon, J.A.; O'Hara, J.; Booth, J.; Smith, D.R. An Overview of the Theory and Applications of Metasurfaces: The Two-Dimensional Equivalents of Metamaterials. *IEEE Antennas Propag. Mag.* **2012**, *54*, 10–35. [CrossRef]
17. Kildishev, A.V.; Boltasseva, A.; Shalaev, V.M. Planar Photonics with Metasurfaces. *Science* **2013**, *339*, 1232009. [CrossRef] [PubMed]
18. Chen, H.-T.; Taylor, A.J.; Yu, N. A review of metasurfaces: Physics and applications. *Rep. Prog. Phys.* **2016**, *79*, 076401. [CrossRef]
19. Glybovski, S.B.; Tretyakov, S.A.; Belov, P.A.; Kivshar, Y.S.; Simovski, C.R. Metasurfaces: From microwaves to visible. *Phys. Rep.* **2016**, *634*, 1–72. [CrossRef]
20. He, Q.; Sun, S.; Xiao, S.; Zhou, L. High-Efficiency Metasurfaces: Principles, Realizations, and Applications. *Adv. Opt. Mater.* **2018**, *6*, 1800415. [CrossRef]
21. Azad, A.K.; Efimov, A.V.; Ghosh, S.; Singleton, J.; Taylor, A.J.; Chen, H.-T. Ultra-thin metasurface microwave flat lens for broadband applications. *Appl. Phys. Lett.* **2017**, *110*, 224101. [CrossRef] [PubMed]
22. Lin, D.; Holsteen, A.L.; Maguid, E.; Fan, P.; Kik, P.G.; Hasman, E.; Brongersma, M.L. Polarization-independent metasurface lens employing the Pancharatnam-Berry phase. *Opt. Express* **2018**, *26*, 24835. [CrossRef]
23. Ho, J.S.; Qiu, B.; Tanabe, Y.; Yeh, A.J.; Fan, S.; Poon, A.S.Y. Planar immersion lens with metasurfaces. *Phys. Rev. B* **2015**, *91*, 125145. [CrossRef]
24. Epstein, A.; Eleftheriades, G.V. Arbitrary Antenna Arrays Without Feed Networks Based on Cavity-Excited Omega-Bianisotropic Metasurfaces. *IEEE Trans. Antennas Propag.* **2017**, *65*, 1749–1756. [CrossRef]

25. Epstein, A.; Wong, J.P.; Eleftheriades, G.V. Cavity-excited Huygens' metasurface antennas for near-unity aperture illumination efficiency from arbitrarily large apertures. *Nat. Commun.* **2016**, *7*, 1–10. [CrossRef] [PubMed]
26. Chen, M.; Epstein, A.; Eleftheriades, G.V. Design and Experimental Verification of a Passive Huygens' Metasurface Lens for Gain Enhancement of Frequency-Scanning Slotted-Waveguide Antennas. *IEEE Trans. Antennas Propag.* **2019**, *67*, 4678–4692. [CrossRef]
27. Olk, A.E.; Powell, D.A. Huygens Metasurface Lens for W-Band Switched Beam Antenna Applications. *IEEE Open J. Antennas Propag.* **2020**, *1*, 290–299. [CrossRef]
28. Wang, Z.; Ding, X.; Zhang, K.; Ratni, B.; Burokur, S.N.; Gu, X.; Wu, Q. Huygens Metasurface Holograms with the Modulation of Focal Energy Distribution. *Adv. Opt. Mater.* **2018**, *6*, 1800121. [CrossRef]
29. Wan, W.; Gao, J.; Yang, X. Metasurface Holograms for Holographic Imaging. *Adv. Opt. Mater.* **2017**, *5*, 1700541. [CrossRef]
30. Liu, G.; Wang, H.; Jiang, J.; Xue, F.; Yi, M. A High-Efficiency Transmitarray Antenna Using Double Split Ring Slot Elements. *IEEE Antennas Wirel. Propag. Lett.* **2015**, *14*, 1415–1418. [CrossRef]
31. Li, H.; Wang, G.; Liang, J.; Gao, X.; Hou, H.; Jia, X. Single-Layer Focusing Gradient Metasurface for Ultrathin Planar Lens Antenna Application. *IEEE Trans. Antennas Propag.* **2017**, *65*, 1452–1457. [CrossRef]
32. Wu, L.W.; Ma, H.F.; Gou, Y.; Wu, R.Y.; Wang, Z.X.; Wang, M.; Gao, X.; Cui, T.J. High-transmission ultrathin huygens' metasurface with 360 phase control by using double-layer transmitarray elements. *Phys. Rev. Appl.* **2019**, *12*, 024012. [CrossRef]
33. Xue, C.; Lou, Q.; Chen, Z.N. Broadband Double-Layered Huygens' Metasurface Lens Antenna for 5G Millimeter-Wave Systems. *IEEE Trans. Antennas Propag.* **2020**, *68*, 1468–1476. [CrossRef]
34. Kou, N.; Yu, S.; Ding, Z.; Zhang, Z. One-Dimensional Beam Scanning Transmitarray Lens Antenna Fed by Microstrip Linear Array. *IEEE Access* **2019**, *7*, 90731–90740. [CrossRef]
35. An, W.; Xu, S.; Yang, F.; Li, M. A Double-Layer Transmitarray Antenna Using Malta Crosses with Vias. *IEEE Trans. Antennas Propag.* **2016**, *64*, 1120–1125. [CrossRef]
36. Chen, Y.; Chen, L.; Yu, J.-F.; Shi, X.-W. A C-Band Flat Lens Antenna with Double-Ring Slot Elements. *IEEE Antennas Wirel. Propag. Lett.* **2013**, *12*, 341–344. [CrossRef]
37. Xue, C.; Sun, J.; Niu, L.; Lou, Q. Ultrathin Dual-Polarized Huygens' Metasurface: Design and Application. *Ann. Phys.* **2020**, *532*, 2000151. [CrossRef]
38. Wong, J.P.; Selvanayagam, M.; Eleftheriades, G.V. Design of unit cells and demonstration of methods for synthesizing Huygens metasurfaces. *Photonics Nanostruct.-Fundam. Appl.* **2014**, *12*, 360–375. [CrossRef]
39. Wong, J.P.S.; Selvanayagam, M.; Eleftheriades, G.V. Polarization Considerations for Scalar Huygens Metasurfaces and Characterization for 2-D Refraction. *IEEE Trans. Microw. Theory Tech.* **2015**, *63*, 913–924. [CrossRef]
40. Wan, X.; Jia, S.L.; Cui, T.J.; Zhao, Y.J. Independent modulations of the transmission amplitudes and phases by using Huygens metasurfaces. *Sci. Rep.* **2016**, *6*, 25639. [CrossRef]
41. Epstein, A.; Eleftheriades, G.V. Arbitrary power-conserving field transformations with passive lossless omega-type bianisotropic metasurfaces. *IEEE Trans. Antennas Propag.* **2016**, *64*, 3880–3895. [CrossRef]
42. Chen, M.; Abdo-Sánchez, E.; Epstein, A.; Eleftheriades, G.V. Theory, design, and experimental verification of a reflectionless bianisotropic Huygens' metasurface for wide-angle refraction. *Phys. Rev. B* **2018**, *97*, 125433. [CrossRef]
43. Jouanlanne, C.; Clemente, A.; Huchard, M.; Keignart, J.; Barbier, C.; Le Nadan, T.; Petit, L. Wideband Linearly Polarized Transmitarray Antenna for 60 GHz Backhauling. *IEEE Trans. Antennas Propag.* **2017**, *65*, 1440–1445. [CrossRef]
44. Luo, Q.; Gao, S.; Sobhy, M.; Yang, X. Wideband Transmitarray with Reduced Profile. *IEEE Antennas Wirel. Propag. Lett.* **2018**, *17*, 450–453. [CrossRef]
45. Holloway, C.L.; Mohamed, M.A.; Kuester, E.F.; Dienstfrey, A. Reflection and transmission properties of a metafilm: With an application to a controllable surface composed of resonant particles. *IEEE Trans. Electromagn. Compat.* **2005**, *47*, 853–865. [CrossRef]
46. Epstein, A.; Eleftheriades, G.V. Huygens' metasurfaces via the equivalence principle: Design and applications. *J. Opt. Soc. Am. B* **2016**, *33*, A31. [CrossRef]
47. Al-Joumayly, M.A.; Behdad, N. Wideband Planar Microwave Lenses Using Sub-Wavelength Spatial Phase Shifters. *IEEE Trans. Antennas Propag.* **2011**, *59*, 4542–4552. [CrossRef]

48. Li, M.; Behdad, N. Wideband True-Time-Delay Microwave Lenses Based on Metallo-Dielectric and All-Dielectric Lowpass Frequency Selective Surfaces. *IEEE Trans. Antennas Propag.* **2013**, *61*, 4109–4119. [CrossRef]
49. Oh, J. Millimeter-Wave Thin Lens Employing Mixed-Order Elliptic Filter Arrays. *IEEE Trans. Antennas Propag.* **2016**, *64*, 3222–3227. [CrossRef]
50. Wang, Z.X.; Wu, J.W.; Wan, X.; Wu, L.W.; Xiao, Q.; Cheng, Q.; Cui, T.J. Broadband and ultrathin Huygens metasurface with high transmittance. *J. Phys. D Appl. Phys.* **2020**, *53*, 455102. [CrossRef]

Publisher's Note: MDPI stays neutral with regard to jurisdictional claims in published maps and institutional affiliations.

© 2020 by the authors. Licensee MDPI, Basel, Switzerland. This article is an open access article distributed under the terms and conditions of the Creative Commons Attribution (CC BY) license (http://creativecommons.org/licenses/by/4.0/).